

Space Variant Representations for Mobile Platform Vision Applications

Naveen Onkarappa and Angel D. Sappa

Computer Vision Center, Edifici O, Campus UAB,
08193 Bellaterra, Barcelona, Spain
{naveen,asappa}@cvc.uab.es

Abstract. The log-polar space variant representation, motivated by biological vision, has been widely studied in the literature. Its data reduction and invariance properties made it useful in many vision applications. However, due to its nature, it fails in preserving features in the periphery. In the current work, as an attempt to overcome this problem, we propose a novel space-variant representation. It is evaluated and proved to be better than the log-polar representation in preserving the peripheral information, crucial for on-board mobile vision applications. The evaluation is performed by comparing log-polar and the proposed representation once they are used for estimating dense optical flow.

Keywords: log-polar mapping, space-variant representation, optical flow.

1 Introduction

Space variant representation schemes have been used in the computer vision field in order to improve the efficiency of proposed solutions. *Log-Polar Representation* (LPR) is one of the most widely used. It is inspired by the biological vision systems [1], [2] and has been exploited in the robotics and active vision communities for pattern recognition [3] and navigation [4] tasks. The LPR has many advantages with respect to the conventional cartesian representation of images [5]; the most important are the reduction in the data and invariance to scale and rotation. The data reduction due to the polar mapping and logarithmic sub-sampling leads to a high resolution in the fovea and a low resolution in the periphery, which is a desired feature for instance in the active vision community.

A review of log-polar imaging is presented in [6] for robotic vision applications such as: visual attention, target tracking and 3D perception. All these applications benefit from the high resolution of the fovea region. There have been also attempts to use LPRs for motion analysis [4] [7], mainly based on the estimation of optical flow. For instance, [5] presents the advantages of polar and log-polar mapping to the cartesian representation and proposes a technique to estimate time-to-impact using optical flow. In [8], a novel optical flow computation approach is proposed. It is based on the concept of variable window and generalized dynamic image model. The variable window adapts its size along the LP space. Also working in the LP space, [9] analyzes the polar deformation and proposes several local optical flow estimation techniques on log-polar plane.

In the particular contexts of robotics and advanced driver assistance systems (ADAS), LPR has attracted the attention of many researchers. In general, in these fields LPRs are obtained using the *vanishing point* (VP) as a center of the log-polar reference system. $VP_{(x,y,z)}$ corresponds to a point at $z \rightarrow \infty$ where two parallel lines of a road appear to converge in the image plane. Since LPR results in a high sampling in the fovea region, the periphery are under-sampled. It should be noted that the periphery corresponds to regions near to the camera reference system, hence are the most important areas for robotics navigation tasks and ADAS applications. Furthermore, features near to the camera are not only useful for detection tasks but also for an accurate calibration; note that the accuracy of 3D data decreases with the depth.

In the current work a new space variant representation scheme is proposed. It is intended to overcome the problem of LPR with respect to periphery in forward facing motion problems. The superiority of the proposed representation, to LPR, is analyzed using dense optical flow on these representations. The paper is organized as follows. Section 2 presents the proposed space variant representation and optical flow estimation. Then, experimental results and a comparative study are given in Section 3. Finally, the work is concluded in Section 4.

2 Proposed Approach

This section introduces first, the LPR and then the proposed space variant representation of cartesian images; next, the basic variational optical flow model is presented.

2.1 Space-Variant Representations

A log-polar representation is a polar mapping with logarithmic distance along the radial axis. For a given pixel (x, y) , the log-polar (ρ, θ) are defined as:

$$\rho = \log(\sqrt{(x - x_0)^2 + (y - y_0)^2}), \quad \theta = \arctan((y - y_0)/(x - x_0)), \quad (1)$$

where (x_0, y_0) is the origin of mapping; the current work focuses on the study of the particular scenario of forward facing moving platforms, hence the origin of the reference system corresponds to the vanishing point.

As mentioned above, LPR oversamples the fovea and undersamples the periphery. This leads to the non-preservation of vital information of the periphery useful for mobility applications. The latter motivates us to propose a better space variant representation, where a (x, y) pixel is mapped as:

$$\rho = \log(r_{max} - \sqrt{(x - x_0)^2 + (y - y_0)^2}), \quad \theta = \arctan((y - y_0)/(x - x_0)), \quad (2)$$

where r_{max} is the radius of the largest inner circle around VP in the cartesian image. This is different from LPR in the sense that logarithmic subsampling is from the periphery towards the center and will be referred as *Reverse Log-Polar Representation* (RLPR). Figure 1 (*right*) shows LP (*top*) and RLP (*bottom*) representations of the same image Fig. 1(*left*). In both cases the images are sparsely

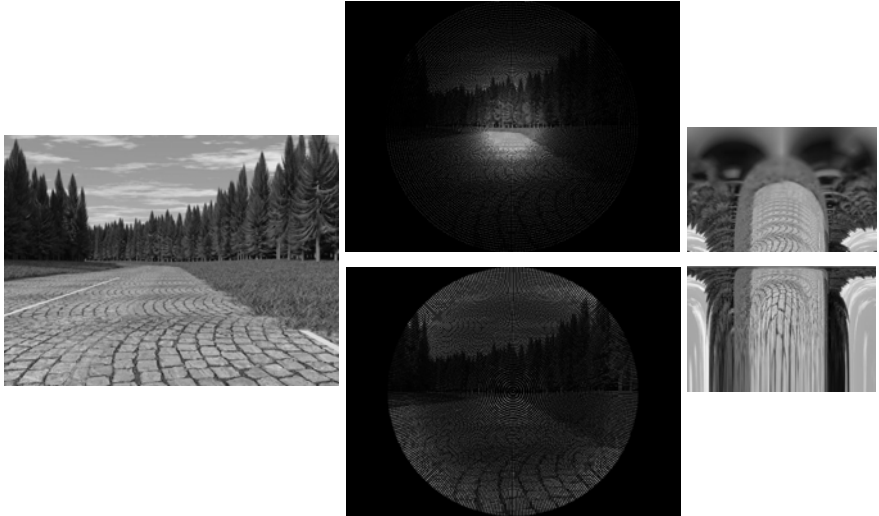


Fig. 1. (top) Log-Polar and (bottom) Reverse-Log-Polar representations of an image

sampled as depicted in Fig. 1(*middle*) correspondingly. Since the LP/RLP transformation involves both many-to-one and one-to-many mapping, the LP/RLP images cannot be straight forwardly dense. The dense images presented in the right column are obtained by querying for each (ρ, θ) to the cartesian and by bilinear interpolations—horizontal axis is angles (θ 's) and vertical axis is distances (ρ 's). As can be seen in the grids in Fig. 1(*middle*), qualitatively, the RLPR image better preserves the periphery information, which covers most part of the road at the bottom in the scenario of a moving vehicle.

2.2 Variational Optical Flow

The aim in this paper is to evaluate the performance of LP and RLP representations once they are used to compute optical flow in the context of on-board vision systems. The variational optical flow [10] is based on two assumptions: *i*) the *brightness constancy* (BCA) and *ii*) the homogeneous regularization. The BCA, also called as *optical flow constraint*, assumes the grey value of objects remains constant over time. The homogeneous regularization assumes that the resulting flow field varies smoothly all over the image, necessary to overcome the aperture problem. The BCA can be formulated as: $I_1(\mathbf{x} + \mathbf{u}) - I_0(\mathbf{x}) = 0$, where I_0 and I_1 is the image pair, $\mathbf{x} = (x_1, x_2)$ is the pixel location within a rectangular image domain $\Omega \subseteq \mathbf{R}^2$; $\mathbf{u} = (u_1(\mathbf{x}), u_2(\mathbf{x}))$ is the two-dimensional displacement vector. Linearizing above equation using first-order Taylor expansion, and combining it with smoothness assumption in a single variational framework and squaring both constraints, the energy functional becomes:

$$E(\mathbf{u}) = \int_{\Omega} \left\{ \underbrace{(I_{x_1} u_1 + I_{x_2} u_2 + I_t)^2}_{Data\ Term} + \alpha \underbrace{(|\nabla u_1|^2 + |\nabla u_2|^2)}_{Regularization} \right\} d\mathbf{x}, \quad (3)$$

where α is a regularization parameter. Variational optical flow energy functions can be minimized in a number of ways. The most used way is to express and solve the set of Euler-Lagrange equations of the energy model. Another popular way of solving eq. (3) is by using a dual formulation based on iterative alternating steps [11]. In the current work a recent variational optical flow technique [12] is used. It explores the basic formulation and some concepts such as pre-processing, coarse-to-fine warping, graduated non-convexity, interpolation, derivatives, median filtering. [12] proposes an improved model underlying median filtering.

3 Experimental Results

As mentioned in Section 1, there have been many applications using LP represented images, some of them based on the optical flow estimation on those images. The current work aims to estimate the optical flow on RLP represented images and compare it with results from LPRs.

In LP/RLP representations of images the origin of mapping should be the vanishing point in the scenario of a forward facing moving vehicle, so that the mapped images better suit the applications. In the current work, vanishing points computed from a RANSAC based approach [13] are used. Then, the optical flow is computed on these LP and RLP represented images. The bottleneck to compare the flow fields from LP and RLP representations is that the flow field patches at a particular location in both representations correspond to different regions of the image in cartesian with varied resolution. Hence, the framework proposed to perform the comparison consists of inverse mapping the flow fields back to cartesian and compare them in the cartesian space. Figure 2 shows an image pair in cartesian (*top-left*), their ground-truth flow (*top-right*), LPR (*middle-left*) and RLPR (*bottom-left*), and their computed flow fields (*middle-right* and *bottom-right*). The color map used to display optical flow is shown in Fig. 2 bottom right corner. Since the image pairs correspond to a translation along the camera focal axis, the flow field in cartesian looks diverging. The computed flow field in both LP/RLP representations looks blue in color indicating all the vectors point downwards. Figure 3 depicts the inverse maps of both LP and RLP flow fields back to cartesian which are sparse. Hereinafter, the LP and RLP representations of flow fields refer to these mapped back to cartesian.

The well known error measures to compare flow fields are Average Angular Error (AAE) and Average End-Point error (AEP) [14] [15]. The AAE is chosen in the current work as the measure to compare flow fields. The angular error e between two vectors (u_1, v_1) and (u_2, v_2) is given by:

$$e((u_1, v_1), (u_2, v_2)) = \arccos \left(\frac{u_1 u_2 + v_1 v_2 + 1}{\sqrt{(u_1^2 + v_1^2 + 1)(u_2^2 + v_2^2 + 1)}} \right). \quad (4)$$

Since the flow fields from LP and RLP representations are sparse and of varied resolution, in order to do a fair comparison a common set of pixels (mask) is selected. Figure 4 shows the masks of LPR (*left*) and RLPR (*middle*) of flow

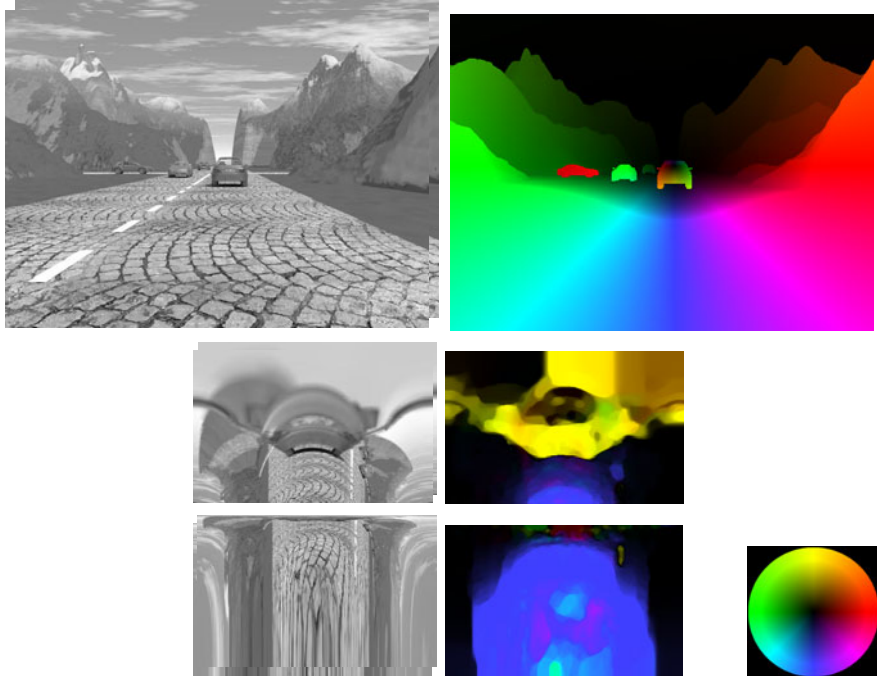


Fig. 2. (top) Flow fields in Cartesian, (middle) LP and (bottom) RLP representations

fields and the intersection mask (*right*) that is the set of positions those have flow values in both representations. This mask is used to compute the errors between LPR/RLPR and ground-truth flow fields. Table 1 shows AAE of ten different flow fields from sequence-1 of set-2 of [16]. The images in this dataset are of resolution 480×640 . They are mapped to LP and RLP representations of resolution 230×360 , placing the vanishing point at $(230, 340)$, computed from [13]. Then, optical flow is computed on these images using [12]. The flow fields are mapped back to cartesian and then, using the mask as shown in Fig. 4(*right*), the AAEs between LP and ground-truth flow fields, and between RLP and ground-truth flow fields, are computed. The AAEs in Table 1 show that flow fields estimated in RLP representations are more accurate than flow fields from LPRs. In all these experiments, the image region contained in the largest inner circle around the vanishing point is considered for mapping to LP/RLP.

Table 1. AAEs (deg.) for flow fields from sequences [16] in LPR and RLPR

		1	2	3	4	5	6	7	8	9	10
Seq. 1	LPR	24.38	24.35	23.99	23.95	23.92	23.80	23.63	23.78	23.53	23.42
	RLPR	20.98	19.15	19.04	19.43	18.30	18.47	18.47	18.00	17.92	18.94
Seq. 2	LPR	24.30	24.59	27.45	27.18	24.32	24.63	24.70	24.52	24.75	24.87
	RLPR	21.68	21.80	27.24	26.60	21.61	23.39	24.25	23.80	23.87	22.05

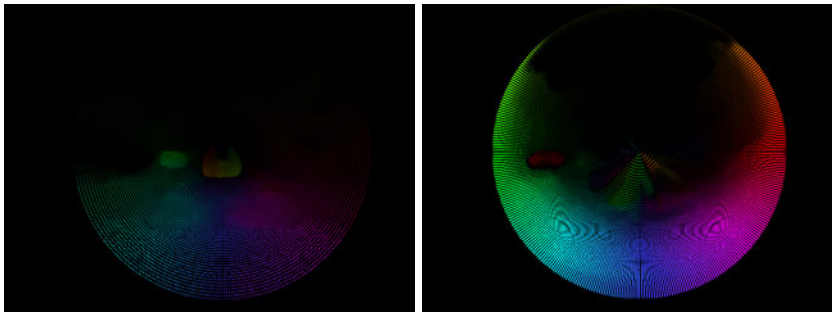


Fig. 3. Inverse mapped flow fields from (*left*) LP and (*right*) RLP

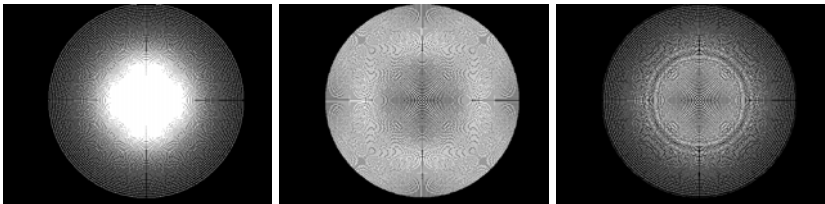


Fig. 4. (*left*) LP mask; (*middle*) RLP mask; (*right*) Mask from their intersection

A similar experiment on sequence-2 of set-2 of [16] is performed; results are presented in Table 1. Vanishing point for these 10 image pairs lies in (240, 320), and the resolution of the mapped images is 240×360 . In the results of sequence-2, the difference in AAEs between LP and RLP is smaller than the results of sequence-1 because the displacement between consecutive frames in sequence-2 is very high. These large displacements lead to more stretching in RLP represented images and hence more erroneous flow fields.

Further experiments are done to analyze how the error evolves along the space in these variant representations. Different circular regions around the vanishing point, with an increase in the radius of the circles within the flow field boundary, are considered. At each radius of the circle, the AAE is calculated inside the circle and outside the circle. This experiment is done on both LPR and RLPR. Since the radial axis for the flow fields of sequence-1 of set-2 is of length 230, nine circles with increasing radius from 23 till 207 in multiples of 23 are considered. Figure 5(*top-left*) and (*middle-left*) shows the AAEs in colormap for the region inside the circle at radius of 115 for LPR and RLPR. Figure 5(*top-right*) and (*middle-right*) show the AAEs in colormap for the region outside the circle at radius 115 for LPR and RLPR respectively. In Fig. 5(*bottom-left*), solid lines indicates AAEs (the average of ten flow fields' region inside the circle) with the increase in radius in LPR. The AAE increases as the inner area increases with the increase in radius. This proves that the flow field near the fovea is more accurate than in the periphery in LPR. The dashed lines correspond to AAEs (the average of ten flow fields' region inside the circle) in RLPRs with

the increase in radius. In the plot Fig. 5(*bottom-left*) the AAE of RLPR decreases from radius 138 till the boundary. At radius 207, where most of the image area is covered inside the circle, the AAE of RLPR is less than the AAE of LPR. This shows RLPR is better at periphery than LPR.

Figure 5(*bottom-right*) shows the AAEs of LPR and RLPR, outside the circles, with the increase in radii of the circles. That means the outer area getting reduced with the increase in radius of the circle. The solid line indicating AAE of LPR increases as the outer area decreases, whereas the dashed line indicating AAE of RLPR decreases as the outer area decreases till the circle with radius 161. Then it increases due to some artifacts in the extreme periphery of RLPR flow field. Figure 5(*middle-right*) shows the artifact, thin band of circular arc on the top, whereas this band is absent in the LPR (*top-right*) flow field. This plot (*bottom-right*) gives the same conclusion obtained from the plot in (*bottom-left*).

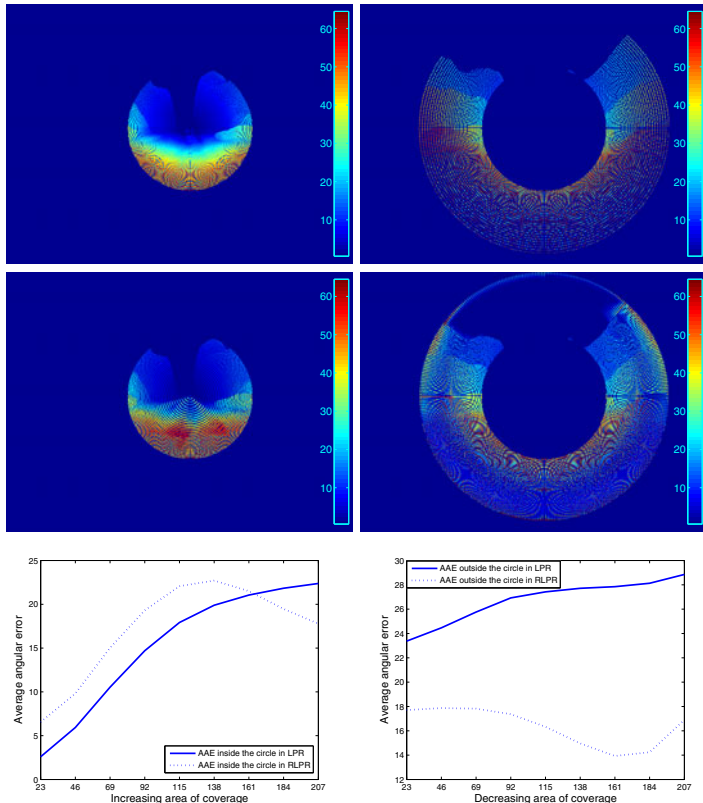


Fig. 5. Analysis of AAEs over space in LPR and RLPR (values in colormap scale computed from eq. 4). (*left*) Region inside circle. (*right*) Region outside circle.

4 Conclusion

The current paper shows that LPR, although inspired by biological vision systems, is not an appropriate representation for forward faced on-board vision systems, where translation in the optical axis is the predominant motion (e.g., mobile robotics, automotives). The previous statement is proved in a dense optical flow estimation framework, using as evaluation metric the average angular error. The optical flow is estimated on both, LP and RLP representations, and the results qualitative and quantitatively shows RLPR better preserves the peripheral information and hence more accurate flow field. The analysis of variance of errors along the space proves that the accuracy in flow field decreases along the distance from the fovea in LPR, whereas it increases along the distance from the fovea to periphery in RLPR. The possible future works are estimation of vanishing point along with the optical flow estimation in proposed representation, analysis of data reduction in RLPR to LPR and the cause of errors in space variant representations.

Acknowledgements. This work was supported by the Spanish govt. under Project TRA2010-21371-C03-01 and Research Program Consolider Ingenio 2010: MIPRCV (CSD2007-00018). The FI grant of AGAUR, Catalan govt. supports the first author.

References

1. Bolduc, M., Levine, M.D.: A review of biologically motivated space-variant data reduction models for robotic vision. *Computer Vision and Image Understanding* 69(2), 170–184 (1998)
2. Schwartz, E.L., Greve, D.N., Bonmassar, G.: Space-variant active vision: Definition, overview and examples. *Neural Networks* 8(7-8), 1297–1308 (1995)
3. Traver, V.J., Pla, F.: The log-polar image representation in pattern recognition tasks. In: Perales, F.J., Campilho, A.C., Pérez, N., Sanfeliu, A. (eds.) IbPRIA 2003. LNCS, vol. 2652, pp. 1032–1040. Springer, Heidelberg (2003)
4. Daniilidis, K.: Computation of 3-d-motion parameters using the log-polar transform. In: Hlaváč, V., Šára, R. (eds.) CAIP 1995. LNCS, vol. 970, pp. 82–89. Springer, Heidelberg (1995)
5. Tistarelli, M., Sandini, G.: On the advantages of polar and log-polar mapping for direct estimation of time-to-impact from optical flow. *IEEE Trans. Pattern Anal. Mach. Intell.* 15(4), 401–410 (1993)
6. Traver, V.J., Bernardino, A.: A review of log-polar imaging for visual perception in robotics. *Robotics and Autonomous Systems* 58(4), 378–398 (2010)
7. Traver, V.J., Pla, F.: Motion analysis with the radon transform on log-polar images. *Journal of Mathematical Imaging and Vision* 30(2), 147–165 (2008)
8. Yeasin, M.: Optical flow in log-mapped image plane-a new approach. *IEEE Trans. Pattern Anal. Mach. Intell.* 24(1), 125–131 (2002)
9. Daniilidis, K., Krüger, V.: Optical flow computation in the log-polar-plane. In: Hlaváč, V., Šára, R. (eds.) CAIP 1995. LNCS, vol. 970, pp. 65–72. Springer, Heidelberg (1995)

10. Horn, B.K.P., Schunk, B.G.: Determining optical flow. *Artificial Intelligence* 17, 185–203 (1981)
11. Zach, C., Pock, T., Bischof, H.: A duality based approach for realtime $TV-L^1$ optical flow. In: Hamprecht, F.A., Schnörr, C., Jähne, B. (eds.) DAGM 2007. LNCS, vol. 4713, pp. 214–223. Springer, Heidelberg (2007)
12. Sun, D., Roth, S., Black, M.J.: Secrets of optical flow estimation and their principles. In: CVPR, pp. 2432–2439 (2010)
13. Onkarappa, N., Sappa, A.D.: On-board monocular vision system pose estimation through a dense optical flow. In: Campilho, A., Kamel, M. (eds.) ICIAR 2010. LNCS, vol. 6111, pp. 230–239. Springer, Heidelberg (2010)
14. Baker, S., Scharstein, D., Lewis, J.P., Roth, S., Black, M.J., Szeliski, R.: A database and evaluation methodology for optical flow. In: ICCV, pp. 1–8 (2007)
15. Barron, J.L., Fleet, D.J., Beauchemin, S.S.: Performance of optical flow techniques. *International Journal of Computer Vision* 12(1), 43–77 (1994)
16. Vaudrey, T., Rabe, C., Klette, R., Milburn, J.: Differences between stereo and motion behaviour on synthetic and real-world stereo sequences. In: Proc. Image and Vision Computing, Christchurch, New Zealand, pp. 1–6 (2008)